Biomechanics and Modeling in Mechanobiology
https://doi.org/10.1007/s10237-019-01214-5

ORIGINAL PAPER

Modelling the electrical activity of skeletal muscle tissue using a multi-domain approach

Thomas Klotz[1,2] · **Leonardo Gizzi**[1,2] · **Utku Ş. Yavuz**[1,3] · **Oliver Röhrle**[1,2]

Received: 27 March 2019 / Accepted: 17 August 2019

Abstract
Electromyography (EMG) can be used to study the behaviour of the motor neurons and thus provides insights into the physiology of the central nervous system. However, due to the high complexity of neuromuscular control, EMG signals are challenging to interpret. While the exact knowledge of the excitation patterns of a specific muscle within an in vivo experimental setting remains elusive, simulations allow to systematically investigate EMG signals in a controlled environment. Within this context, simulations can provide virtual EMG data, which, for example, can be used to validate and optimise signal analysis methods that aim to estimate the relationship between EMG signals and the output of motor neuron pools. However, since existing methods, which are employed to compute EMG signals, exhibit deficiencies with respect to the physical model itself as well as with respect to numerical aspects, we propose a novel homogenised continuum model that closely resolves the electro-physiological behaviour of skeletal muscle tissue. The proposed model is based on an extension of the well-established bidomain model and includes a biophysically detailed description of the electrical activity within the tissue, which is due to the depolarisation of the muscle fibre membranes. In contrast to all other published EMG models, which assume that the electrical potential field for each muscle fibre can be calculated independently, the proposed model assumes that the electrical potential in the muscle fibres is coupled to the electrical potential in the extracellular space. We show that the newly proposed model is able to simulate realistic EMG signals and demonstrate the potential to employ the predicted virtual EMG signal in order to evaluate the goodness of automated decomposition algorithms.

Keywords EMG · Biophysical · Bidomain · Multi-scale · Decomposition algorithms · Motor units

1 Introduction

Skeletal muscles can be voluntarily controlled by the somatic nervous system in order to generate force and motion. The underlying physiological pathways rely on specialised control strategies and on interconnected functional structures (cf. e.g. Kandel et al. 2000; MacIntosh et al. 2006). A motor unit (MU), which is the smallest functional unit that can be controlled individually, consists of a motor neuron and all muscle fibres that are innervated by the motor neuron. The fact that a muscle is composed of several (up to hundreds) MUs results in a broad variation in activation patterns. The large number of MUs is necessary to finely modulate the force output and therefore enables complex motion. Thus, in order to improve the knowledge of both physiological and pathophysiological neuromuscular control strategies, it is essential to identify the recruitment patterns of the MUs. The overall electrical activity of skeletal muscles can be measured by means of electromyography (EMG) (Merletti and Parker 2004) and, therefore,

✉ Thomas Klotz
thomas.klotz@machbau.uni-stuttgart.de

Leonardo Gizzi
leonardo.gizzi@mechbau.uni-stuttgart.de

Utku Ş. Yavuz
s.u.yavuz@utwente.nl

Oliver Röhrle
roehrle@simtech.uni-stuttgart.de

[1] Institute for Modelling and Simulation of Biomechanical Systems, Pfaffenwaldring 5a, 70569 Stuttgart, Germany

[2] Stuttgart Centre for Simulation Science (SimTech), Pfaffenwaldring 5a, 70569 Stuttgart, Germany

[3] Biomedical Signals and Systems, Universiteit Twente, 7500AE Enschede, Netherlands

Published online: 16 September 2019

serves as a window into the physiology of the neuromuscular system. However, due to the complex recruitment principles of skeletal muscles, the muscle tissue properties itself, and inherent measurement limitations, experimentally recorded EMG signals are often challenging to interpret. For example, separating the contributions of different MUs from the interference EMG signal is a complex mathematical problem that often yields incomplete results (Holobar et al. 2010). In detail, due to the high number of unknowns (e.g. the complex muscle geometry, changes in tissue conductivity due to, for example, changes in a subject's hydration, neural and muscular fatigue, and so on), it is nearly impossible to establish and validate a univocal relationship between the acquired signal and the output of motor neuron pools, i.e. the recruitment patterns generated by the motor neurons innervating a specific muscle. In this context, modelling the electrical properties of skeletal muscle tissue allows to systematically investigate the characteristics of (virtual) EMG signals in a controlled environment and as such represents a method which can importantly contribute to a better understanding of the neuromuscular system. In particular, the possibility to use synthetic EMG data to test the accuracy and, hence, the validity of different signal processing and classification strategies, as well as to evaluate the effects of specific electrode arrangements, is promising.

There exist multiple models that aim to compute EMG signals. Essentially all existing models assume that skeletal muscle tissue can be modelled as a lumped volume conductor, whereby the (local) depolarisation of the muscle fibre membranes (sarcolemma) can be represented by means of a current source (for a review, see Mesin 2013). Depending on the complexity of the geometry, the muscle architecture, and/or spatial heterogeneities of the tissue properties, such volume conductor models can be either solved analytically (cf. e.g. Farina and Merletti 2001; Mesin 2005) or have to be discretised by means of the finite difference method or the finite element method and then solved numerically (cf. e.g. Dimitrova et al. 1999; Lowery et al. 2002, 2004; Farina et al. 2004; Mesin et al. 2006; Mordhorst et al. 2015). While volume conductor models have been used to analyse the spatial filtering effect of tissue architectures and to analyse EMG signals during non-isometric contractions (Mordhorst et al. 2015), the decoupled and therefore simplified representation the bio-electrical sources requires some a priori assumptions (e.g. on the propagating properties of the action potentials in the muscle fibres) that potentially limit the accuracy of volume conductor models. Further, the representation of the bio-electrical sources on the fibre scale requires a fine spatial resolution, leading to high computational costs (Carriou et al. 2018; Mordhorst et al. 2017).

In addition to the above-mentioned phenomenological volume conductor models, there exists the bidomain model (Miller and Geselowitz 1978; Tung 1978) that represents a biophysically motivated continuum modelling approach for simulating electrically active tissues. Thereby, the bidomain model is particularly popular to predict the electrical potential fields within the heart (Clayton et al. 2011; Henriquez 1993). One advantage of the bidomain model is that it provides, in contrast to the above-mentioned modelling approaches, the possibility to include a more detailed and consistent description of the electrical activity (cf. e.g. Keener and Sneyd 2009; Pullan et al. 2005). As such, the bidomain model is a continuum modelling approach for which one assumes that both intracellular and extracellular spaces coexist at the same material point, i.e. yielding a homogenised two-domain medium, whereby both domains are electrically coupled by balancing the flow of ions across the cell membrane. Due to its ability to include a biophysically detailed description of the membrane, the bidomain model is considered within the electrophysiology community as the gold standard. Note that in the special case of equal anisotropy ratios of the conductivity in both the intracellular and the extracellular spaces, the bidomain model can be simplified, i.e. yielding the monodomain model (cf. e.g. Keener and Sneyd 2009). Even though this assumption does typically not hold, the monodomain model is often used as computationally cheaper approximation of the more detailed bidomain model (cf. e.g. Huang et al. 1999; Nielsen et al. 2007; Sundnes et al. 2006). Besides the above described common two-domain approach, there also exist modifications of the bidomain model. For example, Buist and Poh (2010) and Corrias et al. (2012) proposed a more general form of the bidomain model by taking into account not only one but two different cell types. This is needed, for example, to appropriately simulate the propagation of electrical waves in the gastrointestinal tract.

However, none of the existing bidomain-like models is capable of adequately resolving the electro-physiological behaviour of skeletal muscle tissue. In detail, while the classical bidomain model fails to resolve the specialised anatomo-physiological architecture of skeletal muscle tissue, i.e. incorporate its organisation in MUs, existing extensions of the bidomain model fail to resolve the propagating properties of action potentials within the muscle fibres. Thus, volume conductor models are typically used to simulate the electrical potential fields within skeletal muscle tissue originating from muscular activity. Thereby, in contrast to biophysically more detailed modelling approaches, the electrical potential filed within each fibre has to be precomputed and used as source term in the volume conductor model. However, the underlying assumption justifying the use of precomputed electrical potentials as source terms within volume conductor models, i.e. the electrical potential field within the muscle fibres is independent from the electrical state of the extracellular space, is a simplification that can yield modelling errors, which have never been investigated or quantified. Further, the representation of the electrical sources on the fibre scale requires an exact knowledge of all fibre positions and their

associated motor neuron. This, however, is not feasible with state-of-the-art in vivo imaging techniques. Moreover, the discrete modelling of idealised muscle fibres leads to jumps in the electrical potential that can be compared to phase transitions between different intracellular domains. This yields a strong mesh dependency of the mathematical model and thus leading to the conclusion that the representative elementary volume is not appropriately chosen for volume conductor models (cf. e.g. Geers et al. 2017; Hill 1963).

To overcome these limitations, we propose an extension of the bidomain model, the so-called multi-domain model, that takes into account the characteristic functional structure of skeletal muscle tissue (cf. Sect. 2.2) and, therefore, is capable of simulating realistic EMG signals (cf. Sect. 3.1 to 3.4). Further, we demonstrate the possibility to use simulated EMG signals to evaluate the quality of automated decomposition algorithms (cf. Sect. 3.4).

2 Methods

Skeletal muscle tissue is a heterogeneous material consisting of muscle fibres associated with different MUs and extracellular matrix (cf. Fig. 1). To adequately model the anatomo-physiological structure of skeletal muscle tissue within a multi-scale continuum modelling approach, the microscopic architecture of the tissue is taken into account in an averaged sense, while macroscopically it is assumed that there coexist at each material point an extracellular space and one individual intracellular space per modelled MU. This can be considered to be a generalisation of the well-established bidomain model. Like for the bidomain model, it is assumed that ions can flow from each intracellular domain into the extracellular space while we do not allow for any current flux between the different intracellular domains. More specifically, we assume that each MU can be represented by one muscle fibre and consider its interaction with the adjoined extracellular space, i.e. yielding a representative fibre–matrix cylinder (cf. Fig. 1). Further, conservation of charges at the macroscopic material point is guaranteed by taking into account the microscopic composition of the tissue. Following those assumptions and employing suitable constitutive relations, one can derive a system of coupled partial differential equations (PDEs) that can be used to describe the electrophysiological properties of skeletal muscle tissue. The derivation of the entire model is outlined in the following.

2.1 The electrostatic equations

The EMG signal can be considered as a measure of the electrical potential field induced by depolarisation of the muscle fibre membranes. In classical electromagnetism, the evolution of electric and magnetic fields is described by Maxwell's equations. Based on the assumption that the electric and magnetic fields change relatively slowly over time, i.e. for skeletal muscle tissue the stimulation frequencies are typically lower than 100 Hz, one can use the electrostatic approximation to decouple the electric and the magnetic fields. For this case, the quasi-static electrical field equations are summarised by Gauss's law, Faraday's law, and the affiliated conservation of charges (cf. e.g. Griffiths 2013), i.e. by

$$\operatorname{div} \boldsymbol{e} = \frac{v}{\varepsilon_0}, \quad \operatorname{curl} \boldsymbol{e} = 0 \quad \text{and} \quad \operatorname{div} \boldsymbol{j} = 0, \tag{1}$$

where $\operatorname{div}(\cdot)$ and $\operatorname{curl}(\cdot)$ denote the divergence and curl operator, respectively, $\boldsymbol{e}$ is the electrical field intensity, v is the

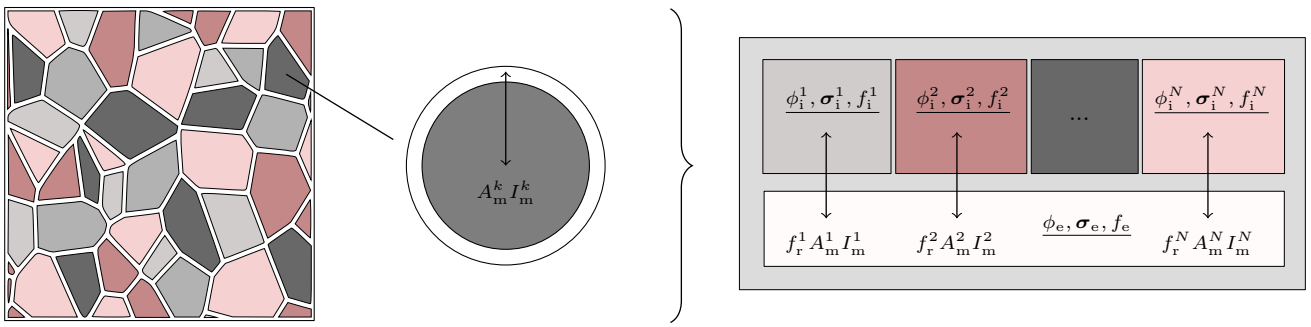

Fig. 1 Left: Schematic drawing of skeletal muscles microstructure. More specifically, the figure shows a cross-sectional area of muscle tissue (orthogonal to the fibre direction) consisting of multiple fibres belonging to different MUs (indicated by different colours). The fibres are surrounded by the extracellular space (white). Middle: Instead of considering the actual geometry of a fibre, one assumes that each fibre within the fully resolved, microstructural geometry can be represented by an idealised cylindrical fibre. Further, to simulate the electrical coupling between the muscle fibres and the extracellular space, the model considers the interaction of one representative fibre for each MU and the neighbouring extracellular space, i.e. yielding a representative fibre–matrix cylinder for all intracellular domains. Right: Illustration of the homogeneity assumption, i.e. each skeletal muscle material point considers one extracellular space and one intracellular domain per MU. Electrically, the extracellular domain is coupled to all intracellular domains by the weighted transmembrane current densities I_{m}^{k}, whereby the model takes into account the microscopic composition of the tissue

electrical charge density, ε_0 is the vacuum permittivity, and $\boldsymbol{j}$ denotes the macroscopic current density. Starting from the quasi-static electrical field equations, we will introduce suitable modelling assumptions to simulate the electro-physiological behaviour of skeletal muscle tissue.

2.2 Modelling the electro-physiological properties of skeletal muscle tissue

It is assumed that at each material point within muscle tissue $\mathcal{P} \in \Omega_\mathrm{m}$ an extracellular and N intracellular domains, where N is the number of MUs (cf. Fig. 1), coexist. We assume that the different muscle domains are electrically coupled and that ions can only flow from an intracellular space into the extracellular space, but not between the different intracellular domains. Therefore, an individual electrical potential is defined for each domain, i.e. ϕ_e and ϕ_i^k ($\forall\, k \in \mathscr{M}_\mathrm{MU} := \{1, 2, \dots, N\}$), where the subscripts $(\cdot)_\mathrm{e}$ and $(\cdot)_\mathrm{i}$ denote extracellular and intracellular quantities, respectively. In addition, one can introduce for each MU k, with $k \in \mathscr{M}_\mathrm{MU}$, a transmembrane potential

$$V_\mathrm{m}^k \;=\; \phi_\mathrm{i}^k \;-\; \phi_\mathrm{e}\,. \tag{2}$$

Furthermore, the electrical properties of the domains are characterised by the conductivity tensors $\boldsymbol{\sigma}_\mathrm{e}$ and $\boldsymbol{\sigma}_\mathrm{i}^k$ ($\forall\, k \in \mathscr{M}_\mathrm{MU}$), i.e. which can reflect anisotropic tissue properties.

Assuming that ions can only flow from an intracellular domain into the extracellular space and in the absence of additional current sources and sinks, any current that is leaving the intracellular domain associated with MU k ($\forall\, k \in \mathscr{M}_\mathrm{MU}$) must enter the extracellular space via the transmembrane current density I_m^k. From a mathematical point of view, the conservation of charges at each material point can be enforced by relating the outward volume fluxes from each domain and the transmembrane current densities I_m^k. Thereby, based on homogenisation, we take into account the microscopic composition and the microscopic architecture of skeletal muscle tissue in an averaged sense. In detail, assuming that the interaction between the intracellular domains and the extracellular space can be modelled by considering a representative fibre–matrix cylinder (cf. Fig. 1), the outward volume current flux from a representative muscle fibre into the adjoined extracellular space is calculated for each intracellular space k, with $k \in \mathscr{M}_\mathrm{MU}$, by

$$\mathrm{div}\boldsymbol{j}_\mathrm{i}^k \;=\; A_\mathrm{m}^k I_\mathrm{m}^k\,, \quad \text{in } \Omega_\mathrm{m}\,. \tag{3}$$

Further, the outward volume current flux from the extracellular space is calculated by taking into account the weighted transmembrane current densities from all MUs, i.e.

$$\mathrm{div}\boldsymbol{j}_\mathrm{e} \;=\; -\sum_{k=1}^{N} f_\mathrm{r}^k A_\mathrm{m}^k I_\mathrm{m}^k\,, \quad \text{in } \Omega_\mathrm{m}\,. \tag{4}$$

Therein, $\boldsymbol{j}_\mathrm{e}$ is the current density in the extracellular space and $\boldsymbol{j}_\mathrm{i}^k$ ($\forall\, k \in \mathscr{M}_\mathrm{MU}$) denotes the current densities of the intracellular spaces. Further, A_m^k ($\forall\, k \in \mathscr{M}_\mathrm{MU}$) is the membrane surface per representative fibre–matrix cylinder volume, i.e. reflecting an averaged shape parameter of the muscle fibres geometries, and f_r^k is a microstructural parameter taking into account the composition of the tissue which is defined as

$$f_\mathrm{r}^k \;=\; f_\mathrm{i}^k \,/\, \sum_{j=1}^{N} f_\mathrm{i}^j\,. \tag{5}$$

There in, f_i^k ($\forall\, k \in \mathscr{M}_\mathrm{MU}$) denotes the volume fractions of the respective intracellular spaces, i.e. describing the probability that an arbitrary point within a representative control volume belongs to a specific phase. Thereby, note that, in order to ensure physical consistency, we require the sum of all volume fractions to be equal to 1, i.e. yielding for each macroscopic material point $\mathcal{P} \in \Omega_\mathrm{m}$

$$f_\mathrm{e} \;+\; \sum_{k=1}^{N} f_\mathrm{i}^k \;=\; 1\;, \tag{6}$$

whereby f_e denotes the volume fraction of the extracellular space. Further note that the transmembrane current densities I_m^k need to be specified by an additional constitutive relation [cf. Eq. (9)].

Moreover, it is assumed that the relation between the electrical field intensity and the current density can be described by Ohm's law, i.e. $\boldsymbol{j} = \boldsymbol{\sigma}\boldsymbol{e}$, where $\boldsymbol{\sigma}$ is the (spatially varying) conductivity tensor. Since the electrical field is irrotational [cf. Eq. (1)], one can derive the electrical field intensity from a scalar potential field, i.e. $\boldsymbol{e} = -\,\mathrm{grad}\,\phi$. Inserting Eq. (3) into Eq. (4) and exploiting the introduced assumptions yield for each material point $\mathcal{P} \in \Omega_\mathrm{m}$

$$\begin{aligned}
&\mathrm{div}\boldsymbol{j}_\mathrm{e} \;+\; \sum_{k=1}^{N} f_\mathrm{r}^k \mathrm{div}\boldsymbol{j}_\mathrm{i}^k \;=\; 0\\
&\quad\Leftrightarrow\; \mathrm{div}\big[\boldsymbol{\sigma}_\mathrm{e}\mathrm{grad}\,\phi_\mathrm{e}\big]\\
&\qquad +\; \sum_{k=1}^{N} f_\mathrm{r}^k \mathrm{div}\big[\boldsymbol{\sigma}_\mathrm{i}^k \mathrm{grad}\,\phi_\mathrm{i}^k\big] \;=\; 0\\
&\quad\Leftrightarrow\; \mathrm{div}\big[\boldsymbol{\sigma}_\mathrm{e}\mathrm{grad}\,\phi_\mathrm{e}\big]\\
&\qquad +\; \sum_{k=1}^{N} f_\mathrm{r}^k \mathrm{div}\big[\boldsymbol{\sigma}_\mathrm{i}^k \mathrm{grad}\,\big(V_\mathrm{m}^k + \phi_\mathrm{e}\big)\big] \;=\; 0\\
&\quad\Leftrightarrow\; \mathrm{div}\left[\left(\boldsymbol{\sigma}_\mathrm{e} + \sum_{k=1}^{N} f_\mathrm{r}^k \boldsymbol{\sigma}_\mathrm{i}^k\right)\mathrm{grad}\,\phi_\mathrm{e}\right]\\
&\qquad +\; \sum_{k=1}^{N} f_\mathrm{r}^k \mathrm{div}\big[\boldsymbol{\sigma}_\mathrm{i}^k \mathrm{grad}\, V_\mathrm{m}^k\big] \;=\; 0\,.
\end{aligned} \tag{7}$$

Note, Eq. (7) relates the change of the extracellular potential to the depolarisation of the fibre membranes and is equivalent to the conservation of charges at each macroscopic material point [cf. Eq. (1)]. Analogously, we obtain from Eq. (3) $\forall\, k \in \mathscr{M}_{\mathrm{MU}}$

$$\begin{aligned} \operatorname{div} \boldsymbol{j}_{\mathrm{i}}^{k} &= A_{\mathrm{m}}^{k}\, I_{\mathrm{m}}^{k}\,, \quad \text{in } \Omega_{\mathrm{m}}\,, \\ \Leftrightarrow \operatorname{div}\left[\boldsymbol{\sigma}_{\mathrm{i}}^{k} \operatorname{grad} \phi_{\mathrm{i}}^{k}\right] &= A_{\mathrm{m}}^{k}\, I_{\mathrm{m}}^{k}\,, \quad \text{in } \Omega_{\mathrm{m}}\,, \\ \Leftrightarrow \operatorname{div}\left[\boldsymbol{\sigma}_{\mathrm{i}}^{k} \operatorname{grad}\left(V_{\mathrm{m}}^{k} + \phi_{\mathrm{e}}\right)\right] &= A_{\mathrm{m}}^{k}\, I_{\mathrm{m}}^{k}\,, \quad \text{in } \Omega_{\mathrm{m}}\,. \end{aligned} \tag{8}$$

To close the set of equations, it is assumed that the ionic current, which flows across the muscle fibre membrane, is calculated by using a biophysically motivated model that describes the muscle fibre membrane as an electrical equivalent circuit, i.e. employing the biophysical modelling approach introduced by Hodgkin and Huxley (1952). Thus, the overall transmembrane current density I_{m}^{k} for each MU k, with $k \in \mathscr{M}_{\mathrm{MU}}$, is given by the following set of ordinary differential equations:

$$\begin{aligned} I_{\mathrm{m}}^{k}(t) &= C_{\mathrm{m}}^{k} \frac{\partial V_{\mathrm{m}}^{k}(t)}{\partial t} + I_{\mathrm{ion}}^{k}(\boldsymbol{y}^{k}(t), V_{\mathrm{m}}^{k}(t), I_{\mathrm{stim}}^{k}(t))\,, \\ \dot{\boldsymbol{y}}^{k}(t) &= \boldsymbol{g}^{k}(\boldsymbol{y}^{k}(t), V_{\mathrm{m}}^{k}(t))\,, \\ \boldsymbol{y}_{0}^{k} &= \boldsymbol{y}^{k}(t=0)\,, \\ V_{\mathrm{m},0}^{k} &= V_{\mathrm{m}}^{k}(t=0)\,. \end{aligned} \tag{9}$$

Therein, t is the time and C_{m}^{k} is the membrane capacitance of a muscle fibre belonging to MU k, which is assumed to be constant for each MU. Further, $\boldsymbol{g}^{k}(\boldsymbol{y}^{k}(t), V_{\mathrm{m}}^{k}(t))$ is a multi-dimensional function describing the dynamics of the fibre membrane associated with MU k (for example, the gating dynamics of the ion channels), $I_{\mathrm{ion}}^{k}(\boldsymbol{y}^{k}(t), V_{\mathrm{m}}^{k}(t), I_{\mathrm{stim}}^{k}(t))$ is the ionic current flowing over all ion channels and pumps of the fibre membranes associated with MU k, and $I_{\mathrm{stim}}^{k}(t)$ is an external stimulus that will be used to describe the motor nerve firing sequence of MU k at the neuromuscular junctions. Note that for a classical Hodgkin–Huxley type model, i.e. neglecting flow of ions along the spatial coordinates and thus reflecting a closed electrical circuit, the overall transmembrane current density I_{m}^{k} is equal to zero. Further note that for the sake of compactness, the arguments of the individual functions are omitted in the following.

Finally, combining Eqs. (9) and (8) yields $\forall\, k \in \mathscr{M}_{\mathrm{MU}}$

$$\begin{aligned} \frac{\partial V_{\mathrm{m}}^{k}}{\partial t} &= \frac{1}{C_{\mathrm{m}}^{k} A_{\mathrm{m}}^{k}} \big(\operatorname{div}\left[\boldsymbol{\sigma}_{\mathrm{i}}^{k} \operatorname{grad} V_{\mathrm{m}}^{k}\right] \\ &\quad + \operatorname{div}\left[\boldsymbol{\sigma}_{\mathrm{i}}^{k} \operatorname{grad} \phi_{\mathrm{e}}\right] - A_{\mathrm{m}}^{k} I_{\mathrm{ion}}^{k}(\boldsymbol{y}^{k}, V_{\mathrm{m}}^{k})\big)\,, \quad \text{in } \Omega_{\mathrm{m}}, \end{aligned} \tag{10a}$$

$$\dot{\boldsymbol{y}}^{k} = \boldsymbol{g}^{k}(\boldsymbol{y}^{k}, V_{\mathrm{m}}^{k})\,, \quad \text{in } \Omega_{\mathrm{m}}. \tag{10b}$$

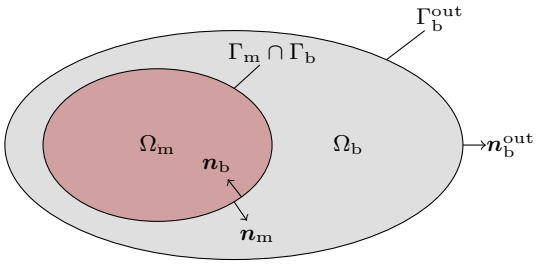

Fig. 2 Schematic drawing representing an arbitrary geometrical arrangement of muscle tissue (red) and surrounding electrically inactive tissue (grey) to illustrate the different regions and their coupling / boundary interfaces

In summary, Eqs. (7) and (10a) form a system of $(N+1)$ coupled partial differential equations that are strongly linked to a set of ordinary differential equations [cf. Eq. (10b)]. Note that for $N = 1$, the model exactly coincides with the bidomain model.

2.3 Modelling electrically inactive tissue

In the body, skeletal muscle tissue is surrounded by bone, connective, adiposes, and skin tissue, whereby all of them can be assumed to be electrically inactive. Nevertheless, the electrical properties of the surrounding tissue affect the measured EMG signals, i.e. acting as spatial filter, and therefore should be taken into account. In the following, we refer to all electrically inactive tissues as body region and denote them by Ω_{b}. Electrically inactive tissues, i.e. reflecting tissues that are free of current sources, can be modelled as a lumped volume conductor (cf. e.g. Mesin 2013; Pullan et al. 2005). Accordingly, the electrical behaviour of the body region can be described by a generalised Laplace equation, i.e.

$$\operatorname{div}\left[\boldsymbol{\sigma}_{\mathrm{b}} \operatorname{grad} \phi_{\mathrm{b}}\right] = 0\,, \quad \text{in } \Omega_{\mathrm{b}}\,, \tag{11}$$

where $\boldsymbol{\sigma}_{\mathrm{b}}$ is the (spatially varying) conductivity tensor in the body region and ϕ_{b} is the electrical potential in the body region.

2.4 Boundary and interface conditions

To close the system of coupled partial differential equations formed by Eqs. (7), (10a), and (11), suitable boundary conditions need to be introduced. Like for the bidomain equations, it is assumed that no current can flow over the outer boundary of the body region. This leads to zero Neumann boundary conditions, i.e.

$$\left[\boldsymbol{\sigma}_{\mathrm{b}} \operatorname{grad} \phi_{\mathrm{b}}\right] \cdot \boldsymbol{n}_{\mathrm{b}}^{\mathrm{out}} = 0\,, \quad \text{on } \Gamma_{\mathrm{b}}^{\mathrm{out}}\,, \tag{12}$$

where "$\cdot$" denotes the scalar product and $\boldsymbol{n}_{\mathrm{b}}^{\mathrm{out}}$ is the unit outward normal vector with respect to the outer body surface

$\Gamma_{\mathrm{b}}^{\mathrm{out}}$ (cf. Fig. 2). Further, at the interface between the muscle region and the body region, it is assumed that the extracellular potential, ϕ_{e}, is equal to the potential in the body region, ϕ_{b}, and that the current, which leaves the extracellular space, must enter the body region, i.e.

$$\phi_{\mathrm{e}} = \phi_{\mathrm{b}}\,, \qquad \text{on } \Gamma_{\mathrm{m}} \cap \Gamma_{\mathrm{b}} \text{ and} \tag{13a}$$

$$\begin{aligned} &\left[\boldsymbol{\sigma}_{\mathrm{e}} \mathrm{grad}\, \phi_{\mathrm{e}}\right] \cdot \boldsymbol{n}_{\mathrm{m}} \\ &\quad = -\left[\boldsymbol{\sigma}_{\mathrm{b}} \mathrm{grad}\, \phi_{\mathrm{b}}\right] \cdot \boldsymbol{n}_{\mathrm{b}}\,, \quad \text{on } \Gamma_{\mathrm{m}} \cap \Gamma_{\mathrm{b}}\,. \end{aligned} \tag{13b}$$

Therein, $\boldsymbol{n}_{\mathrm{m}}$ is the unit outward normal vector with respect to the muscle surface Γ_{m} and $\boldsymbol{n}_{\mathrm{b}}$ is the unit outward normal vector with respect to the body surface Γ_{b} (cf. Fig. 2). Lastly, it is assumed that no current can leave any of the intracellular domains over the boundary of the muscle region Γ_{m}, yielding the following boundary conditions:

$$\begin{aligned} &\left[\boldsymbol{\sigma}_{\mathrm{i}}^{k} \mathrm{grad}\, \phi_{\mathrm{i}}^{k}\right] \cdot \boldsymbol{n}_{\mathrm{m}} = 0\,, \qquad \text{on } \Gamma_{\mathrm{m}}\,, \\ &\quad \Leftrightarrow \left[\boldsymbol{\sigma}_{\mathrm{i}}^{k} \mathrm{grad}\, V_{\mathrm{m}}^{k}\right] \cdot \boldsymbol{n}_{\mathrm{m}} \\ &\quad = -\left[\boldsymbol{\sigma}_{\mathrm{i}}^{k} \mathrm{grad}\, \phi_{\mathrm{e}}\right] \cdot \boldsymbol{n}_{\mathrm{m}}, \quad \text{on } \Gamma_{\mathrm{m}}\,. \end{aligned} \tag{14}$$

However, applying only Neumann-type boundary conditions does not provide a well-posed problem, i.e. solutions could differ by a constant. Therefore, additional Dirichlet boundary conditions are needed. In reality, the additionally needed Dirichlet boundary condition would, for example, be the grounding electrode. Since it is computationally not feasible to simulate the entire body, the domain of interest will be typically restricted to a representative region consisting, for example, of a single muscle or multiple layers of muscle, fat, and skin tissue. Accordingly, in the special case that the muscle surface corresponds to an outer boundary of the simulated region zero Neumann boundary conditions need to be applied on the outer boundary of the muscle with respect to the extracellular potential, i.e.

$$\left[\boldsymbol{\sigma}_{\mathrm{e}} \mathrm{grad} \phi_{\mathrm{e}}\right] \cdot \boldsymbol{n}_{\mathrm{m}} = 0\,, \quad \text{on } \Gamma_{\mathrm{m}} \setminus \Gamma_{\mathrm{b}}\,. \tag{15}$$

2.5 Model parameters

In the intracellular spaces, ions can only flow along the fibre direction. This assumption is based on the physiological property that skeletal muscle fibres have no gap junctions, which would allow ions to flow directly into neighbouring cells. Hence, the intracellular along-the-fibre and transverse-to-the-fibre conductivities were chosen to be $\sigma_{\mathrm{i}}^{\mathrm{f}} = 8.93\mathrm{mS\,cm^{-1}}$ (Bryant 1969) and $\sigma_{\mathrm{i}}^{\mathrm{xf}} = 0.0\mathrm{mS\,cm^{-1}}$, respectively. Thus, the intracellular conductivity tensors for all MUs k (with $k \in \mathscr{M}_{\mathrm{MU}}$) are defined as $\boldsymbol{\sigma}_{\mathrm{i}}^{k} = \sigma_{\mathrm{i}}^{\mathrm{f}}\, \boldsymbol{a} \otimes \boldsymbol{a}$, where $\boldsymbol{a}$ is a unit vector aligned with the muscle fibre direction in the actual configuration. Note, especially when simulating EMG signals during contractions, caution is required with respect to the configuration in which physical quantities are described, i.e. with respect to referential or actual coordinates. Further, the along-the-fibre conductivity of the extracellular space is assumed to be in the same range as for the intracellular space, i.e. $\sigma_{\mathrm{e}}^{\mathrm{f}} = 6.7\,\mathrm{mS\,cm^{-1}}$ (Rush et al. 1963). In contrast to the intracellular space, ions can flow within the extracellular space transverse to the muscle fibre direction (Epstein and Foster 1983). While a wide range of anisotropy ratios has been reported in the literature (cf. e.g. Gabriel et al. 1996; Gielen et al. 1984), within this work we assume an anisotropy ratio of 2 for the extracellular conductivity tensor. Accordingly, the transverse-to-the-fibre conductivity of the extracellular space is given by $\sigma_{\mathrm{e}}^{\mathrm{xf}} = 3.35\,\mathrm{mS\,cm^{-1}}$. The overall extracellular conductivity tensor, $\boldsymbol{\sigma}_{\mathrm{e}}$, can therefore be summarised to read $\boldsymbol{\sigma}_{\mathrm{e}} = \sigma_{\mathrm{e}}^{\mathrm{f}}\, \boldsymbol{a} \otimes \boldsymbol{a} + \sigma_{\mathrm{e}}^{\mathrm{xf}}\, (\boldsymbol{I} - \boldsymbol{a} \otimes \boldsymbol{a})$, where $\boldsymbol{I}$ is the second-order identity tensor. Further, the conductivity of fat tissue is assumed to be isotropic and much lower than the conductivity of muscle tissue. Consequently, we assume for the fat tissue surrounding the muscle a conductivity tensor $\boldsymbol{\sigma}_{\mathrm{b}} = \sigma_{\mathrm{b}} \boldsymbol{I}$ with $\sigma_{\mathrm{b}} = 0.4\,\mathrm{mS\,cm^{-1}}$ (Rush et al. 1963).

To simulate the reaction of the sarcolemma in response to changes of the transmembrane potential or an external stimulus, i.e. to compute I_{m}^{k}, we appeal to the original model of Hodgkin and Huxley (1952). Thereby, the implementation and corresponding initial conditions were adopted from the models repository of the physiome project, i.e. www.cellml.org (Lloyd et al. 2004). Accordingly, the specific membrane capacitance is given by $C_{\mathrm{m}}^{k} = 1\mu\mathrm{F\,cm^{-2}}$ and was assumed to be constant for all MUs. Note that even though the Hodgkin and Huxley (1952) model was originally developed to simulate action potentials in the axon of the squid and does not specifically represent the behaviour of a skeletal muscle fibre membrane, its universal action potential shape is nevertheless a suitable choice to approximate the membrane dynamics within a generic muscle. If another description of the skeletal muscle fibre membranes is desired, the Hodgkin and Huxley (1952) model can be replaced by such a model straight forwardly. Thereby, depending on the desired application, either a biophysical (cf. e.g. Adrian et al. 1970; Cannon et al. 1993; Shorten et al. 2007) or a phenomenological (cf. e.g. FitzHugh 1961) membrane model can be employed.

Further, the average radius of a muscle fibre is correlated with the size of the corresponding motor neuron and the number of fibres belonging to a MU (cf. Del Vecchio et al. 2017). Hence, as far as the membrane surface per representative fibre–matrix cylinder volume, A_{m}^{k}, is concerned, we assume A_{m}^{k} to depend on the size of the MU. Assuming that the total volume fraction of all intracellular spaces is much bigger than the volume fraction of the extracellular space and that the muscle fibres are ideal cylinders, the membrane

surface per representative fibre–matrix cylinder volume can be approximated by $A_{\mathrm{m}}^k \approx 2/r^k$, where r^k is the average radius of a muscle fibre belonging to MU k. For example, given an average fibre radius of $r^k = 40\mu\mathrm{m}$ the corresponding membrane surface per representative fibre–matrix cylinder volume is $A_{\mathrm{m}}^k = 500\ \mathrm{cm}^{-1}$.

2.6 Numerical treatment/discretisation

In general, there exits no analytic solution for the resulting system of differential equations. Therefore, numerical methods need to be applied. Similar to the mathematical characteristics of the bidomain or monodomain model, Eq. (10a) denotes a reaction–diffusion equation. For such equations, it is often convenient to first apply an operator splitting method before employing a discretisation scheme. In detail, operator splitting allows one to separate the nonlinear reaction terms from the corresponding diffusive parts (cf. e.g. Qu and Garfinkel 1999; Sundnes et al. 2005; Whiteley 2006). Hence, applying to the set of equations given by Eq. (10a), i.e. for all $k \in \mathscr{M}_{\mathrm{MU}}$, a first-order Godunov-type splitting before employing first-order finite difference approximations for the temporal derivatives, one obtains equations that are still continuous in Ω_{m} with respect to its spatial variable but already time discretised with a timestep $\Delta t := t_{i+1} - t_i$, i.e.

$$\frac{V_{\mathrm{m}}^{k,t_*} - V_{\mathrm{m}}^{k,t_i}}{\Delta t} = -\frac{1}{C_{\mathrm{m}}^k} I_{\mathrm{ion}}^k(\boldsymbol{y}^k, V_{\mathrm{m}}^k)\,, \tag{16a}$$

$$\frac{V_{\mathrm{m}}^{k,t_{i+1}} - V_{\mathrm{m}}^{k,t_*}}{\Delta t} = \frac{1}{C_{\mathrm{m}}^k A_{\mathrm{m}}^k}\left(\mathrm{div}\left[\boldsymbol{\sigma}_{\mathrm{i}}^k \mathrm{grad}\, V_{\mathrm{m}}^k\right] + \mathrm{div}\left[\boldsymbol{\sigma}_{\mathrm{i}}^k \mathrm{grad}\, \phi_{\mathrm{e}}\right]\right)\,, \tag{16b}$$

where t_* denotes an intermediate timestep. In this way, specialised solution methods can be utilised for the solution of the reactive and diffusive terms of the model equations.

The proposed model was implemented in MATLAB (2016). In detail, Eqs. (10b) and (16a) form a system of stiff coupled ordinary differential equations, which was solved in the interval $[t_i, t_*]$ using MATLAB's built-in solver ODE15s, i.e. of variable step and variable order (Shampine and Reichelt 1997), with an absolute and relative tolerance of 10^{-4} and a maximal step size of 0.1 ms. To solve the diffusive parts of the coupled system of partial differential equations with respect to the associated boundary conditions, i.e. Eqs. (7), (11)–(14), and (16b), the finite difference method was applied to discretise the spatial derivatives. Here, a central finite difference scheme is employed. The discrete representation of the right-hand side of Eqs. (7) and (16b) is evaluated at $t = t_{i+1}$, yielding an implicit Euler method. By following these discretisation steps, one obtains a linear system of the type $\boldsymbol{Mx} = \boldsymbol{Db}$, where

$$\boldsymbol{M} = \left(\begin{array}{ccccc|cc} \boldsymbol{A}_{V_{\mathrm{m}}^1} & & & & & \boldsymbol{A}_{\phi_{\mathrm{e}},1} & \\ & \boldsymbol{A}_{V_{\mathrm{m}}^2} & & & & \boldsymbol{A}_{\phi_{\mathrm{e}},2} & \\ & & \ddots & & & \vdots & \\ & & & \boldsymbol{A}_{V_{\mathrm{m}}^N} & & \boldsymbol{A}_{\phi_{\mathrm{e}},N} & \\ \hline \boldsymbol{B}_{V_{\mathrm{m}}^1} & \boldsymbol{B}_{V_{\mathrm{m}}^2} & \cdots & \boldsymbol{B}_{V_{\mathrm{m}}^N} & & \boldsymbol{B}_{\phi_{\mathrm{e}}} & \boldsymbol{B}_{\phi_{\mathrm{b}}} \\ \hline & & & & & \boldsymbol{C}_{\phi_{\mathrm{e}}} & \boldsymbol{C}_{\phi_{\mathrm{b}}} \end{array}\right), \tag{17}$$

$$\boldsymbol{x} = \begin{pmatrix} \boldsymbol{V}_{\mathrm{m}}^{1,t_{i+1}} \\ \boldsymbol{V}_{\mathrm{m}}^{2,t_{i+1}} \\ \vdots \\ \boldsymbol{V}_{\mathrm{m}}^{N,t_{i+1}} \\ \boldsymbol{\Phi}_{\mathrm{e}}^{t_{i+1}} \\ \boldsymbol{\Phi}_{\mathrm{b}}^{t_{i+1}} \end{pmatrix} \quad \text{and} \quad \boldsymbol{b} = \begin{pmatrix} \boldsymbol{V}_{\mathrm{m}}^{1,t_*} \\ \boldsymbol{V}_{\mathrm{m}}^{2,t_*} \\ \vdots \\ \boldsymbol{V}_{\mathrm{m}}^{N,t_*} \\ \boldsymbol{0} \\ \boldsymbol{0} \end{pmatrix}.$$

This system is solved using MATLAB's built-in GMRES solver with the following settings: unrestarted method, incomplete LU factorisation as preconditioner, absolute and a relative tolerance of 10^{-12} (Saad and Schultz 1986). Therein, the matrices $\boldsymbol{A}$, $\boldsymbol{B}$, and $\boldsymbol{C}$ represent the discrete approximations of the spatial differential operators of the model equations and the applied boundary conditions, respectively. Further, $\boldsymbol{D}$ is a diagonal matrix of ones and zeros enforcing the applied boundary conditions.

To demonstrate the consistency between the model output and experimental measurements, a portion of muscle tissue was artificially excited and the resulting compound action potential was simulated (for details see Sect. 3). To exclude geometric effects and to facilitate the comparability between the different cases, all simulations were performed on a cube-shaped (half) muscle sample with edge lengths $x = 4.0$ cm, $y = 1.5$ cm, and $z = 1.0$ cm. Further, the muscle fibres were all aligned in parallel with respect to the x-direction (cf. Fig. 3). To guarantee a unique solution, the extracellular potential ϕ_{e}, was set to ground potential at the bottom surface of the sample. As spatial resolution, we choose 20 discretisation points per centimetre. As timestep, we chose $\Delta t = 0.1$ ms. Note that the system of coupled ordinary differential equations simulating the response of the sarcolemma is solved multiple times during one global timestep. Further note that the model output was stored for every fifth timestep.

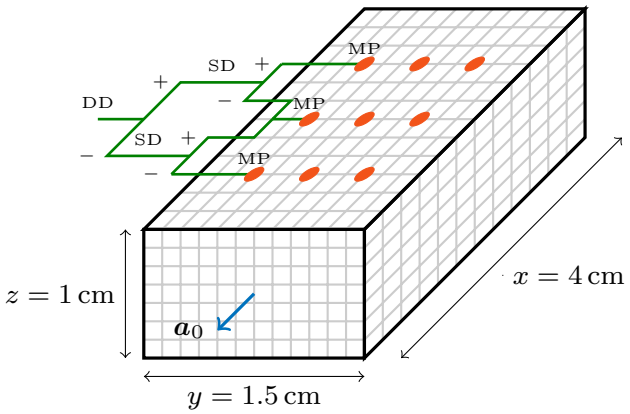

Fig. 3 Schematic representation of the cubic muscle geometry (black lines) and the spatial finite differences discretisation (grey mesh). Thereby, the muscle fibres are assumed to be aligned parallel with the x-axes. The virtual recording points, i.e. the EMG channels, are schematically represented by the red circles. Thereby, the extracellular potential ϕ_e at a specific spatial coordinate can be considered to be equivalent to a monopolar (MP) EMG recording of an idealised point electrode. Further, the monopolar signals from different channels can be combined to calculate the single differential (SD) signals as well as the double differential (DD) signals, respectively

2.7 Data analysis

The extracellular potential ϕ_e predicted by the mathematical model at a given point in space can be considered as equivalent to a referenced monopolar EMG signal, i.e. a signal whose amplitude is measured against a ground reference, detected by an idealised point electrode. Thus, a virtual high-density surface EMG was generated by sampling the extracellular potential ϕ_e at every third grid point of the sample/muscle surface (cf. Fig. 3), yielding for each sampling point a discrete time series of the extracellular potential with a sampling frequency of 2000 Hz. Thereby, note that within the literature the recording points are typically referred to as channels, whereby the temporal content of each channel, sampled at discrete points in time, is referred to as signal. Further, besides the aforementioned referenced monopolar signal, the most commonly used (spatial filtering) recording settings are the single differential and the double differential configuration. In detail, the single differential signal is the output of an operational amplifier whose inputs are two referenced monopolar EMG signals mounted along the muscle fibre direction. Assuming ideal electrodes and an ideal voltmeter, this is equivalent to a sample-by-sample difference of the monopolar signals in two different channels (cf. Fig. 3). Further, the double differential signal refers to the output of an operational amplifier whose inputs are two single differential signals obtained by three referenced monopolar channels with one channel in common (for further details, see Merletti and Parker 2004, Chapter 5). Spatial filtering, i.e. employing a differential recording configuration, improves the quality of sampled signals by reducing the volume of detection and rejecting non-propagating components, i.e. information that appears on multiple recording points at the same time. Thereby, the double differential signal is more spatially selective than the single differential signal.

Classical EMG parameters, such as root mean square (RMS), mean frequency (MNF), and the average muscle fibre conduction velocity (MFCV), were calculated for the virtual high-density EMG signals and used to evaluate the physiological realism of the proposed model. Thereby, RMS and MNF were calculated for arbitrarily chosen single differential derivations of the synthetic surface EMG. In short, the RMS is defined by

$$\mathrm{RMS} = \sqrt{\frac{1}{S}\sum_{i=1}^{S} x_i^2}\,, \tag{18}$$

where S is the number of sampling points (in time) and x_i are the sampled values of an arbitrary signal. The RMS is traditionally used to detect the presence of muscular activity and is considered to reflect changes in the number of recruited MUs and their firing rate. This information is routinely used to label on-off intervals of muscle activity (e.g. for gait analysis) or as a feature for movement classification in myoelectric prostheses control (Merletti and Parker 2004).

Further, the MNF was calculated from an estimate of the power spectral density, i.e. reflecting the squared modulus of a signal's Fourier transform, by utilising MATLAB's built-in meanfreq function. In EMG analysis, MNF is normally computed to detect fatigue during voluntary or electrically elicited contractions and provides indirect evidences for the distribution of activated muscle fibres during isometric contractions (Merletti et al. 2002). In detail, lower RMS and MNF value is expected if the active fibres are located deeper in the muscle or if the thickness of the subcutaneous fat layer increases.

MFCV increases proportionally to the diameter of the active fibres and provides important insights on both MU recruitment and fatigue. Therefore, MFCV was estimated on double differential signals as the ratio between the (spatial) distance of two channels along the fibre direction and their temporal delay. The latter was calculated as the time-shift for which the value of the cross-correlation function between the two signals reaches its absolute maximum (Farina and Merletti 2004). Thereby, the channels were manually selected in a region half way between the innervation zone and the boundary of the simulated muscle. Note that in order to improve the accuracy of the MFCV estimate, real EMG signals are linearly interpolated in time by a factor ranging from 8 to 32 (Farina and Merletti 2004; Gizzi et al. 2008;

Sbriccoli et al. 2009). Therefore, within that work an interpolation factor of 32 was applied on the time-sampled virtual high-density surface EMG to estimate the MFCV.

In order to extract the firing times of the MUs, the virtual high-density surface EMG was decomposed using the commercially available, automatic, HDEMG decomposition tool DEMUSE (V4.5, Maribor University, Slovenia). As decomposition parameters, we chose the number of runs option as "50", the differential option as "yes", a bandpass filter from 20 to 500 Hz, no spatial filtering, and cost function as "standard". The decomposed MUs were visually inspected, and those that exhibited non-physiological firing rate values, i.e. firing rates smaller than 5 pulses per second (PPS) or bigger than 50 PPS, were removed. Isolated firings which were identified as spurious, i.e. those who caused instant spikes in the firing rate of values higher than 100 PPS, were manually removed. To evaluate the quality of the decomposition, the rate of agreement (RoA) between the prescribed and decomposed firings was calculated (Holobar et al. 2010). For each MU k, the RoA is computed by

$$\mathrm{RoA}^k = \frac{A^k}{A^k + P^k + D^k}, \tag{19}$$

where A^k is the total amount of common firings identified, P^k are the firings, which were prescribed but not decomposed, and D^k are the firings identified only in the decomposition but were not prescribed. Common firings were identified as those who appeared in both sets of firings with a maximal delay of ± 0.5 ms (Holobar et al. 2010).

3 Results

To highlight and investigate different properties of the proposed multi-domain model, four different scenarios are selected (Example 1–4). Example 1 (cf. Sect. 3.1) was chosen in such a way that we can analyse the compound action potential of a single MU and the spatial filtering effect of skeletal muscle tissue. To do so, we selectively stimulated a single MU (with an isolated firing) at different muscle tissue depths.

The aim of Example 2 (cf. Sect. 3.2) is to analyse the interference effect arising from the activity of different MUs. Therefore, we simulate two different MUs, which share the same MU territory, i.e. reflecting a subset of the overall muscle volume which is occupied by a specific MU, but exhibit variable firing intervals.

Example 3 (cf. Sect. 3.3) investigates the effect of surrounding adipose tissue. We do so by simulating the compound action potential of an individual MU while varying the thickness of the fat layer on top of the muscle sample. Note that for Examples 1–3, the MUs were stimulated selectively at a virtual neuromuscular junction located at $x = 3.5$ cm, $y = 0.75$ cm, and variable depth. This was done by applying an external stimulation current density $I^k_{\mathrm{stim}} = 700\,\mu\mathrm{A\,cm}^{-2}$ for 0.1 ms and for each firing of the MU k at the stimulation points.

Example 4 (cf. Sect. 3.4) represents a physiologically more realistic scenario. For a population of $N = 10$ MUs, the properties of the MUs were chosen according to basic physiological principles, i.e. the volume of the MU territories as well as the microstructural parameters f^k_{r} of the MUs were chosen proportional to the size of the MU (Henneman et al. 1965). Further, we prescribed a firing rate (ranging from 25 to 7 PPS) and applied a random variable jitter of up to $\pm 10\%$ to the baseline firing rate. Thereby, the neuromuscular junctions were randomly distributed around a plane orthogonal to the muscle fibre direction and $x = 3.5$ cm. The main aim of Example 4 is to demonstrate (1) how the (microscopic) motor unit properties (e.g. the average muscle fibre diameter) relate to macroscopic measurable quantities like MFCV and (2) to illustrate how synthetically generated EMG signals can be used to evaluate the performance of automated signal decomposition methods.

3.1 Example 1: single twitch stimulation

In Example 1, a muscle sample consisting of a single MU, i.e. $N = 1$ with $A^1_{\mathrm{m}} = 500\,\mathrm{cm}^{-1}$ and $f^1_{\mathrm{r}} = 1$, was selectively stimulated (isolated firing) at different depths ($x = 0.5$ cm, $y = 0.5$ cm, $z = [0.1, 0.3, 0.5, 0.7, 0.9]$ cm) within the muscle tissue. For each of the five test scenarios, an individual simulation was initiated. Figure 4 depicts the single differential EMG signal and the corresponding power spectrum at an arbitrarily chosen virtual recording point on the muscle surface, i.e. $x = 0.5$ cm, $y = 0.5$ cm. It can be observed that the amplitude of the time domain signal decreases exponentially with the depth of the activated tissue [cf. Fig.4 (left)], which is reflected by a decrease in RMS (cf. Table 1). This result is qualitatively similar to those obtained in the seminal work of Fuglevand et al. (1992). Further, increasing the depth of the activated muscle fibres leads to smoother time domain signals [cf. Fig.4 (left)], which is emphasised by a shift of

Table 1 Effect of the depth of the activated muscle fibres on the surface EMG signal. The amplitude and the mean frequency decrease exponentially at increasing source depth

Depth (cm)	0.1	0.3	0.5	0.7	0.9
Normalised RMS	1	0.363	0.111	0.036	0.006
Normalised MNF	1	0.834	0.704	0.624	0.590

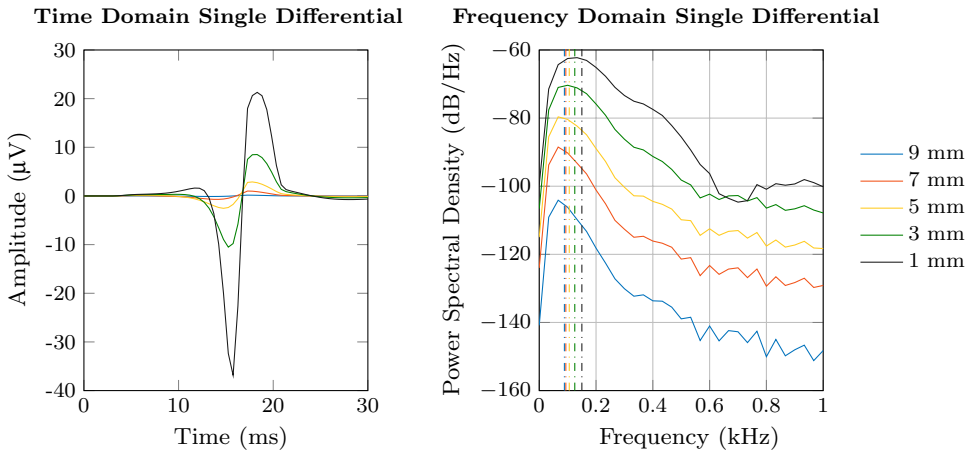

Fig. 4 Time domain graph (left) and frequency spectrum (right) of the simulated single differential surface signal for variable depths of the activated muscle tissue at an arbitrary chosen virtual recording point ($x = 0.5$ cm, $y = 0.5$ cm). The dashed lines in the power spectrum (right) indicate the mean frequency content of the signal

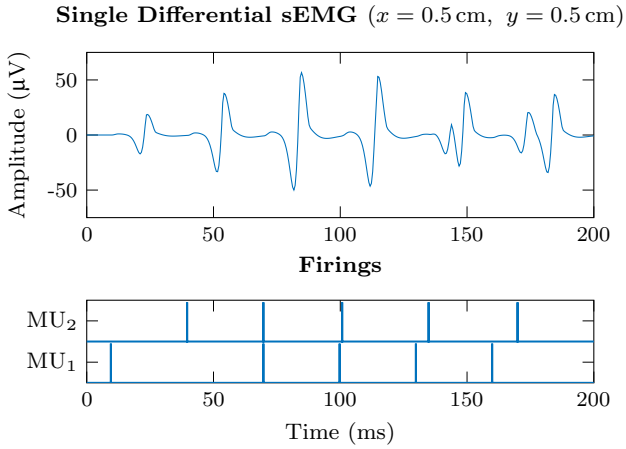

Fig. 5 Effect of constructive and destructive interference at differenet firings of two distinct MUs sharing the same territory. Top: Single differential signal at an arbitrary chosen virtual recording point on the top of the muscle ($x = 0.5$ cm, $y = 0.5$ cm). Bottom: Firing times of both MUs

the mean frequency content to the left, i.e. yielding lower MNF values (cf. Fig. 4 (right) and Table 1). This behaviour demonstrates the presence of an intrinsic low-pass filtering effect of skeletal muscle tissue. Note that both RMS and MNF were normalised with respect to the simulation with the most superficial muscle tissue stimulation (cf. Table 1).

3.2 Example 2: signal summation and cancellation

The focus of Example 2 is to investigate the interplay between two different MUs that share the same territory. As parameters, we choose $A_{\text{m}}^1 = A_{\text{m}}^2 = 500\ \text{cm}^{-1}$, $f_{\text{r}}^1 = 1/3$, and $f_{\text{r}}^2 = 2/3$. Both MUs were stimulated at the same point ($x = 3.5$ cm, $y = 0.75$ cm, $z = 0.5$ cm); however, the temporal interval between the firing times for the two MUs is varied. The exact firing times are depicted in Fig. 5 (bottom). The numerical experiment is examined by analysing the single differential EMG signal at an arbitrary chosen

Table 2 Effect of adipose tissue on the surface EMG signal. Both the amplitude and the mean frequency decrease exponentially if the thickness of the fat tissue increases

Fat thickness (cm)	0	0.25	0.5	0.75
Normalised RMS	1	0.8287	0.5359	0.3471
Normalised MNF	1	0.9675	0.8906	0.8251

point, i.e. at $x = 0.5$ cm and $y = 0.5$ cm, on the muscle surface [cf. Fig. 5 (top)]. Thereby, it can be noticed that the amplitude of the observed EMG signal depends on the size of the MUs, i.e. the microstructural parameter f_{r}^k. Further, depending on the time delay between the firings of the two MUs, constructive or destructive interference can be observed. Note that amplitude cancellation is a well-known phenomenon that influences the reliability of muscular activity estimation, especially at high levels of contraction (Farina et al. 2008).

3.3 Example 3: effect of fat layer thickness

To analyse the impact of surrounding (fat) tissue on the resulting EMG signals, an additional fat layer of variable thickness was modelled. The fat layer was placed on top of the muscle tissue, and the thickness was prescribed as one of the following values: $[0, 0.25, 0.5, 0.75]$ cm. As in Example 1, we consider a single MU, i.e. $N = 1$ with $A_{\text{m}}^1 = 500\ \text{cm}^{-1}$ and $f_{\text{r}}^1 = 1$. The MU was stimulated at $x = 3.5$ cm , $y = 0.75$ cm , $z = 0.5$ cm only once. Thereby, the virtual recording points are always placed on the top surface of the sample (cf. Sect. 2.7). Similar as Example 1, we chose an arbitrary point on the surface, i.e. $x = 0.5$ cm, $y = 0.5$ cm, to analyse the observed single differential EMG signal in the time domain as well as the corresponding power spectrum (cf. Fig. 6). Further, the values of RMS and MNF normalised with respect to the simulation with no fat layer

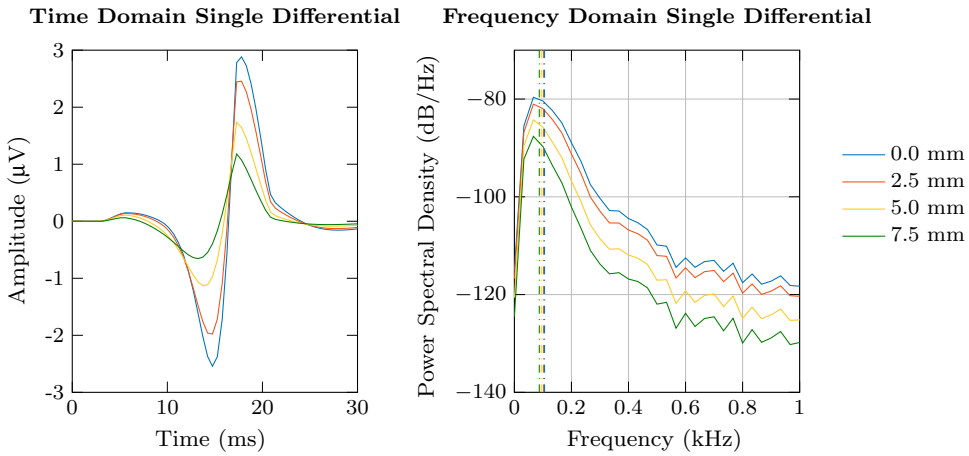

Fig. 6 Time domain graph (left) and frequency spectrum (right) of the simulated signal for variable thicknesses of fat tissue (from 0.0 to 7.5 mm). The dashed lines in the power spectrum (right) indicate the mean frequency content of the signal

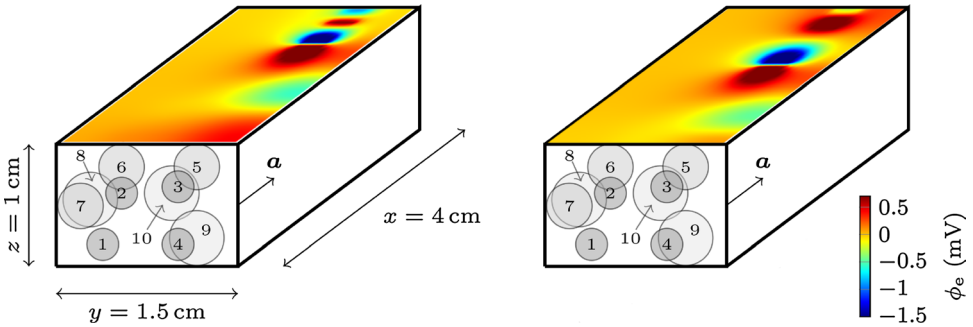

Fig. 7 Illustration of the spatial MU distribution used for Example 4. The figure shows the extracellular potential ϕ_e on the surface of the muscle at two different time frames of the progressive recruitment simulation ($\Delta t = 1$ ms). Note that the empty space can be considered to be occupied by non-active MUs. Thus, by increasing the number of MU, the non-active space would reduce

were calculated and are given in Table 2. The results clearly show a decrease in amplitude of the time domain signal (cf. Fig.6 (left) and Table 2) and a compression of the frequency content (cf. Fig.6 (right) and Table 2), i.e. yielding lower MNF values, with increasing thickness of the fat tissue layer. This behaviour illustrates the low-pass filtering effect of fat tissue on the observed surface EMG.

3.4 Example 4: progressive recruitment

In Example 4, we simulated a population of 10 MUs. Each of the MUs is characterised by a specific firing rate ranging between 25 and 7 PPS, by a volume fraction ranging between approximately 2 % and 18 %, and by a membrane surface per representative fibre–matrix cylinder volume A_m ranging between 500 and 250 cm^{-1}, which corresponds to an average fibre radius between 40 and 80 μm [cf. Table 3)]. The volume of the territories was chosen inversely proportional to the firing rate and is depicted in Fig. 7. Further, the locations of the neuromuscular junctions were normally distributed around a plane orthogonal to the muscle fibre direction and $x = 3.5$ cm. The firing times for each MU were generated by choosing a baseline firing rate (cf. Table 3) and by adding a random jitter of up to ± 10 % to the baseline firing rate.

Table 3 Prescribed average fibre radius, baseline firing rate (FR), and estimated muscle fibres conduction velocities (MFCV) for all MUs

Fibre radius (μm)	Baseline FR (PPS)	MFCV (m/s)
40.00	23.92	2.95
42.35	23.36	2.97
45.00	23.32	3.14
48.00	22.46	3.18
51.42	20.28	3.79
55.38	16.32	3.87
60.0	12.05	3.93
65.45	10.03	4.19
72.0	8.32	4.53
80.0	7.66	5.97

To analyse the effect of the average fibre diameter on the muscle fibre conduction velocity (MFCV), we stimulated each MU individually and estimated the MFCV based on the virtual high-density surface EMG (cf. Sect. 2.7). The

results are depicted in Table 3. Thereby, one can observe that the MFCV increases with the average radius of the muscle fibres, which is in agreement with experimental findings (cf. e.g. Blijham et al. 2006). It is worth noting that this characteristic is not prescribed, but rather appears as a consequence of physiological sound modelling assumptions.

To simulate progressive recruitment, each MU was activated 200 ms after the previous one. The MUs were recruited following the size principle of Henneman et al, i.e. smaller MUs were recruited first. The automatic decomposition with the DEMUSE software as described in Sect. 2.7 yielded 9 MUs. Figure 8 (exemplary) shows a comparison between the prescribed firing times (grey) and the decomposed firing times (black). Thereby, it can be observed that despite slight misalignment of the individual firings, the blind decomposition is able to extract the vast majority of the prescribed firings. Only the MU that was recruited first, i.e. the one with the smallest territory and the smallest amplitude, was not identified by the decomposition algorithm. Quantitatively, the decomposition goodness [cf. Eq. (19)] revealed an average RoA of approximately 99%.

4 Discussion

Within this work, we propose a biophysically detailed, multi-scale model describing the electro-physiological behaviour of skeletal muscle tissue. We show that the newly developed model is able to reproduce key characteristics of experimentally measured EMG signals, i.e. the shape, amplitude, and frequency contents of the individual MU action potentials. Overall, the model respects phenomena like the summation and cancellation of concomitant firings. It reflects the degradation of EMG due to an increase in depth of the source and due to an increase in fat tissue thickness. Further, by employing an automatic decomposition algorithm (DEMUSE), we were able to recover with great precision preselected recruitment patterns. In our example, we were able to recover 9 out of 10 MUs (cf. Sect. 3.4). The one MU, which was not detected, was the MU that was recruited first, i.e. the smallest one. The smallest MU corresponds to the MU with the lowest volume fraction, and the MU is associated with fibres that are located rather deep (cf. Fig. 7). Hence, due to its geometrical location and physiological characteristics, the resulting action potential amplitude at the surface was most likely too small to be detected by the decomposition algorithm. Additionally, the interference through the coupling of different MUs (via the extracellular potential ϕ_e) leads to small variations in the observed compound action potentials of the same MU. This nonlinear system behaviour yields additional complexity for signal separation methods compared to the usually a priori assumed linear system behaviour (as it is, for example, the case for volume conductor models). Therefore, additional investigations are needed to address the influence of the nonlinear system behaviour on the decomposition performance during isometric contractions.

In the future, the proposed model could be used to test and evaluate decomposition algorithms under realistic physiological conditions, i.e. taking into account realistic geometries as well as various recruitment scenarios, and validate the recent development of algorithms which are able to decompose MU firings under dynamic (yet cyclic) contractions, which is not possible with state-of-the-art signal separation methods. In order to achieve that, however, the proposed multi-domain model needs to be included into a

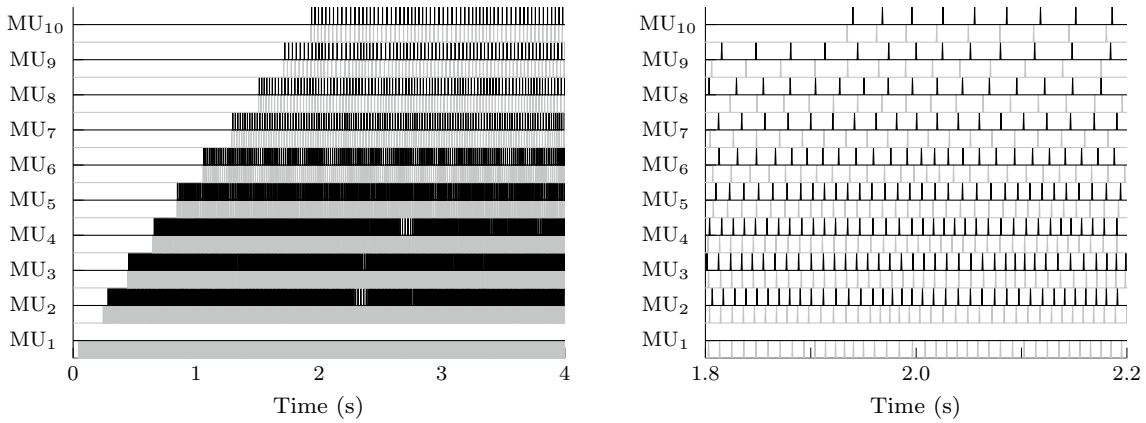

Fig. 8 Prescribed firing times (grey) and decomposed firing times (black) after MU matching. Thereby, the MUs are visualised based on the recruitment order (earliest on the bottom, latest on the top of the figure). Note the figure on the left shows all firings over the entire simulation time while the right figure depicts the same data, however, only from time t = 1.8 s to time t = 2.2 s. It can be noticed that the first MU of the prescribed group was not detected, and therefore, a simple line is shown for the corresponding decomposed MU firing times

multi-physics modelling framework and coupled to a continuum-mechanical skeletal muscle model (e.g. as done in Heidlauf and Röhrle 2013; Mordhorst et al. 2015; Röhrle et al. 2012). Further, by neglecting sensory feedback, e.g. signals originating from muscle spindles, the firing times of the motor neuron pool can be calculated in an independent way and thus enter the skeletal muscle model as a boundary condition. Note we used in this work a simplistic model (based on well-established physiological knowledge) to describe the behaviour of a motor neuron pool during a progressive recruitment scenario. There also exist multiple specialised models that are capable of predicting the discharge times of motor neurons during various conditions (cf. e.g. Fuglevand et al. 1993; Negro and Farina 2011). Further note that even though precomputed discharge times might be sufficient to establish validation data sets for decomposition algorithms, capturing all the features and characteristics of a healthy neuromuscular system in vivo requires the consideration of the sensory system and thus will lead to complex coupled problems (cf. e.g. Röhrle et al. 2019).

In contrast to phenomenological volume conductor models, the propagating properties of the muscle fibre action potentials directly arise from biophysically sound modelling assumptions such as from the interaction between extracellular and intracellular spaces, i.e. by taking into account one representative muscle fibre and the volume fractions for each MU, via the sarcolemma (cf. Sect. 2.2). While no additional modelling assumptions on the conduction velocity of the muscle fibre action potentials are required a priori, the predicted conduction velocities (cf. Table 3) are perfectly in agreement with experimental findings (e.g. Hakansson 1956). Therefore, note that even though such complex biophysical multi-scale models can hardly be validated due to the high number of model parameters, computational experiments as presented herein substantially increase the confidence that the proposed model realistically represents the underling physiological system.

While the proposed multi-domain model is derived by considering a representative muscle fibre and the volume fraction for each MU (cf. Sect.2), a multi-domain approach can also be obtained by homogenising the behaviour of multiple cells (cf. Buist and Poh 2010; Corrias et al. 2012). This would require to consider the membrane surface of all cells belonging to a specific intracellular domain related to the overall control volume to derive the intracellular current balance equations [cf. Eq. (3)]. In a classical bidomain approach, the representative control volume can always be reduced to a single cell interacting with its surrounding extracellular space. Hence, both modelling assumptions will yield the same results. For a multi-domain approach, however, the two different assumptions will result in different biophysical tissue properties. While the conduction velocity of action potentials for the proposed model is strongly associated with the shape of a single cell, for the extended bidomain approach established by Buist and Poh (2010) the conduction velocity of action potentials reflects an ensemble property of multiple cells.

The strictly physics-based modelling approach enables multiple potential applications in the field of applied physiology. For example, the presented model can be used to investigate neuromuscular diseases like myopathies or motor neuron syndromes that are associated with muscle atrophy, in which decreasing muscle fibre diameters eventually causes a reduction in action potential conduction velocity (cf. e.g. Blijham et al. 2006). Such scenarios can be simulated with this model in a straight forward way by adapting, for example, the membrane surface per representative fibre–matrix cylinder volume. Then, the proposed model can be used to evaluate the progress of the disease through its effects on the variables extracted from the EMG signal, e.g. the estimated conduction velocities of the individual MUs. Further, the biophysically detailed description of the membrane also allows to study EMG signals during fatigue, which is caused by accumulation of potassium ions in the T-tubuli system (Mordhorst et al. 2015; Shorten et al. 2007). Moreover, changes of the EMG signals in diseases associated with hyperexcitability of the membrane (e.g. congenital myotonia) can be investigated by altering the ion channels dynamics (Cannon et al. 1993). Utilising the proposed multi-domain approach in a complex, subject-specific model of a residual limb (e.g. such as the ones proposed in Ramasamy et al. 2018), one could significantly decrease patient's time and effort in training myoelectric prostheses control by dramatically increasing the amount of training information and, hence, significantly improving classification-based control. Although all above-mentioned applications aim at simulating the EMG resulting from a voluntary contractions, one could also use this model to accurately calculate the muscular outcomes of functional electrical stimulation paradigms (cf. e.g. Kim et al. 2012; Maffiuletti et al. 2011).

For anatomically complex musculoskeletal systems, the proposed model requires extensive computational resources as one has to solve for an increasingly high number of systems of stiff ordinary differential equations in order to simulate the flow of ionic currents across the membrane. This potentially leads to significant computational costs that require efficient and optimised numerical methods and the use of a highly parallel computing environment (cf. e.g. Bradley et al. 2018). Otherwise, realistic simulations may not be achievable in a reasonable computational time.

In comparison with a volume conductor models, however, the presented homogenised approach proposed herein has several important advantages. As an example, volume conductor models are highly mesh dependent and require an exact knowledge of the muscle fibre arrangement, i.e. each muscle fibre needs to be tracked individually. This is

impossible to obtain from existing in vivo imaging methods. Our proposed approach, on the other hand, only requires knowledge of the muscle fibre direction, which can be measured in vivo, e.g. via diffusion tensor magnetic resonance imaging (DT-MRI) (cf. e.g. Oudeman et al. 2016; Sinha and Yao 2002).

In summary, our multi-domain model consistently integrates skeletal muscle tissues specific physiologically relevant cellular properties within a homogenised, continuum-based, organ-scale model. Hence, for computing in silico predictions of EMG signals, one should use the proposed model instead of existing bidomain-type models or a volume conductor model. Moreover, due to the limiting assumptions of volume conductor or bidomain models, our proposed model could serve as gold standard for simulating EMG and for evaluating motor unit decomposition algorithms.

Acknowledgements This research was funded by the Baden-Württemberg Stiftung as part of the DiHu project of the High Performance Computing II program and by Deutsche Forschungsgemeinschaft (DFG, German Research Foundation) under Germany's Excellence Strategy – EXC 2075 – 390740016.

References

Adrian RH, Chandler WK, Hodgkin AL (1970) Voltage clamp experiments in striated muscle fibres. J Physiol 208(3):607–644

Blijham PJ, Ter Laak HJ, Schelhaas HJ, Van Engelen B, Stegeman DF, Zwarts MJ (2006) Relation between muscle fiber conduction velocity and fiber size in neuromuscular disorders. J Appl Physiol 100(6):1837–1841

Bradley CP, Emamy N, Ertl T, Göddeke D, Hessenthaler A, Klotz T, Krämer A, Krone M, Maier B, Mehl M, Rau T, Röhrle O (2018) Enabling detailed, biophysics-based skeletal muscle models on hpc systems. Front Physiol 9:816. https://doi.org/10.3389/fphys.2018.00816

Bryant SH (1969) Cable properties of external intercostal muscle fibres from myotonic and nonmyotonic goats. J Physiol 204:539–550. https://doi.org/10.1113/jphysiol.1969.sp008930

Buist ML, Poh YC (2010) An extended bidomain framework incorporating multiple cell types. Biophys J 99(1):13–18. https://doi.org/10.1016/j.bpj.2010.03.054

Cannon S, Brown R, Corey D (1993) Theoretical reconstruction of myotonia and paralysis caused by incomplete inactivation of sodium channels. Biophys J 65(1):270–288

Carriou V, Boudaoud S, Laforet J (2018) Speedup computation of hd-semg signals using a motor unit-specific electrical source model. Med Biol Eng Comput 56(8):1459–1473. https://doi.org/10.1007/s11517-018-1784-5

Clayton R, Bernus O, Cherry E, Dierckx H, Fenton FH, Mirabella L, Panfilov AV, Sachse FB, Seemann G, Zhang H (2011) Models of cardiac tissue electrophysiology: progress, challenges and open questions. Prog Biophys Mol Biol 104(1–3):22–48

Corrias A, Pathmanathan P, Gavaghan DJ, Buist ML (2012) Modelling tissue electrophysiology with multiple cell types: applications of the extended bidomain framework. Integr Biol 4(2):192–201

Del Vecchio A, Negro F, Felici F, Farina D (2017) Distribution of muscle fibre conduction velocity for representative samples of motor units in the full recruitment range of the tibialis anterior muscle. Acta Physiol 222(2):e12,930. https://doi.org/10.1111/apha.12930

Dimitrova NA, Dimitrov AG, Dimitrov GV (1999) Calculation of extracellular potentials produced by an inclined muscle fibre at a rectangular plate electrode. Med Eng Phys 21:583–588. https://doi.org/10.1016/S1350-4533(99)00087-9

Epstein BR, Foster KR (1983) Anisotropy in the dielectric properties of skeletal muscle. Med Biol Eng Comput 21(1):51. https://doi.org/10.1007/BF02446406

Farina D, Merletti R (2001) A novel approach for precise simulation of the EMG signal detected by surface electrodes. IEEE Trans Biomed Eng 48:637–646. https://doi.org/10.1109/10.923782

Farina D, Merletti R (2004) Methods for estimating muscle fibre conduction velocity from surface electromyographic signals. Med Biol Eng Comput 42(4):432–445

Farina D, Mesin L, Martina S (2004) Advances in surface electromyographic signal simulation with analytical and numerical descriptions of the volume conductor. Med Biol Eng Comput 42:467–476. https://doi.org/10.1007/BF02350987

Farina D, Cescon C, Negro F, Enoka RM (2008) Amplitude cancellation of motor-unit action potentials in the surface electromyogram can be estimated with spike-triggered averaging. J Neurophysiol 100(1):431–440

FitzHugh R (1961) Impulses and physiological states in theoretical models of nerve membrane. Biophys J 1(6):445–466

Fuglevand AJ, Winter DA, Patla AE, Stashuk D (1992) Detection of motor unit action potentials with surface electrodes: influence of electrode size and spacing. Biol Cybern 67(2):143–153

Fuglevand AJ, Winter DA, Patla AE (1993) Models of recruitment and rate coding organization in motor unit pools. J Neurophys 70(6):2470–2488

Gabriel S, Lau RW, Gabriel C (1996) The dielectric properties of biological tissues: Ii. measurements in the frequency range 10 hz to 20 ghz. Phys Med Biol 41(11):2251

Geers MGD, Kouznetsova VG, Matouš K, Yvonnet J (2017) Homogenization methods and multiscale modeling: nonlinear problems. In: Stein E, de Borst R, Hughes TJR (eds) Encyclopedia of computational mechanics second edition. https://doi.org/10.1002/9781119176817.ecm2107

Gielen FLH, Wallinga-de Jonge W, Boon KL (1984) Electrical conductivity of skeletal muscle tissue: experimental results from different musclesin vivo. Med Biol Eng Comput 22(6):569–577. https://doi.org/10.1007/BF02443872

Gizzi L, Lenti M, Felici F, Filligoi G (2008) Muscle fibers conduction velocity in cycling: a cross correlation-based application for dynamic exercise. In: IET Conference proceedings

Griffiths DJ (2013) Introduction to electrodynamics, 4th edn. Pearson, Boston

Hakansson C (1956) Conduction velocity and amplitude of the action potential as related to circumference in the isolated fibre of frog muscle. Acta Physiol Scand 37(1):14–34

Heidlauf T, Röhrle O (2013) Modeling the chemoelectromechanical behavior of skeletal muscle using the parallel open-source software library open CMISS. Comput Math Methods Med 2013:1–14. https://doi.org/10.1155/2013/517287

Henneman E, Somjen G, Carpenter DO (1965) Functional significance of cell size in spinal motoneurons. J Neurophysiol 28(3):560–580

Henriquez CS (1993) Simulating the electrical behavior of cardiac tissue using the bidomain model. Crit Rev Biomed Eng 21(1):1–77

Hill R (1963) Elastic properties of reinforced solids: some theoretical principles. J Mech Phys Solids 11:357–372

Hodgkin AL, Huxley AF (1952) A quantitative description of membrane current and its application to conduction and excitation in

nerve. J Physiol 117(4):500–544. https://doi.org/10.1113/jphysiol.1952.sp004764
Holobar A, Minetto MA, Botter A, Negro F, Farina D (2010) Experimental analysis of accuracy in the identification of motor unit spike trains from high-density surface emg. IEEE Trans Neural Syst Rehabil Eng 18(3):221–229
Huang Q, Eason JC, Claydon FJ (1999) Membrane polarization induced in the myocardium by defibrillation fields: an idealized 3-d finite element bidomain/monodomain torso model. IEEE Trans Biomed Eng 46(1):26–34
Kandel ER, Schwartz JH, Jessell TM et al (2000) Principles of neural science, vol 4. McGraw-Hill, New York
Keener J, Sneyd J (2009) Mathematical physiology II: cellular physiology, vol 2, 2nd edn. Springer, Berlin
Kim JH, Trew ML, Pullan AJ, Röhrle O (2012) Simulating a dual-array electrode configuration to investigate the influence of skeletal muscle fatigue following functional electrical stimulation. Comput Biol Med 42(9):915–924. https://doi.org/10.1016/j.compbiomed.2012.07.004
Lloyd CM, Halstead MD, Nielsen PF (2004) Cellml: its future, present and past. Prog Biophys Mol Biol 85(2):433–450. https://doi.org/10.1016/j.pbiomolbio.2004.01.004 (Modelling cellular and tissue function)
Lowery MM, Stoykov NS, Taflove A, Kuiken TA (2002) A multiple-layer finite-element model of the surface EMG signal. IEEE Trans Biomed Eng 49(5):446–454. https://doi.org/10.1109/10.995683
Lowery MM, Stoykov NS, Dewald PA, Kuiken TA (2004) Volume conduction in an anatomically based surface EMG model. IEEE Trans Biomed Eng 51:2138–2147. https://doi.org/10.1109/TBME.2004.836494
MacIntosh RB, Gardiner FP, McComas JA (2006) Skeletal muscle: form and function, 2nd edn. Human Kinetics, New York
Maffiuletti NA, Minetto MA, Farina D, Bottinelli R (2011) Electrical stimulation for neuromuscular testing and training: state-of-the art and unresolved issues. Eur J Appl Physiol 111:2391. https://doi.org/10.1007/s00421-011-2133-7
MATLAB (2016) Version 9.0.0.341360 (R2016a). Natick, Massachusetts: The MathWorks Inc
Merletti R, Parker PA (2004) Electromyography: physiology, engineering, and non-invasive applications, vol 11. Wiley, London
Merletti R, Farina D, Gazzoni M, Schieroni MP (2002) Effect of age on muscle functions investigated with surface electromyography. Muscle Nerve 25(1):65–76
Mesin L (2005) Analytical generation model of surface electromyogram for multi-layer volume conductors. Model Med Biol VI WIT 8:95–110. https://doi.org/10.2495/BIO050101
Mesin L (2013) Volume conductor models in surface electromyography: computational techniques. Comput Biol Med 43(7):942–952. https://doi.org/10.1016/j.compbiomed.2013.02.002
Mesin L, Joubert M, Hanekom T, Merletti R, Farina D (2006) A finite element model for describing the effect of muscle shortening on surface EMG. IEEE Trans Biomed Eng 53:600–693. https://doi.org/10.1109/TBME.2006.870256
Miller WT, Geselowitz DB (1978) Simulation studies of the electrocardiogram. I. The normal heart. Circ Res 43(2):301–315. https://doi.org/10.1161/01.RES.43.2.301
Mordhorst M, Heidlauf T, Röhrle O (2015) Predicting electromyographic signals under realistic conditions using a multiscale chemo-electro-mechanical finite element model. Interface Focus 5(2):1–11. https://doi.org/10.1098/rsfs.2014.0076
Mordhorst M, Strecker T, Wirtz D, Heidlauf T, Röhrle O (2017) POD-DEIM reduction of computational EMG models. J Comput Sci 19:86–96. https://doi.org/10.1016/j.jocs.2017.01.009
Negro F, Farina D (2011) Decorrelation of cortical inputs and motoneuron output. J Neurophysiol 106(5):2688–2697
Nielsen BF, Ruud TS, Lines GT, Tveito A (2007) Optimal monodomain approximations of the bidomain equations. Appl Math Comput 184(2):276–290
Oudeman J, Mazzoli V, Marra MA, Nicolay K, Maas M, Verdonschot N, Sprengers AM, Nederveen AJ, Strijkers GJ, Froeling M (2016) A novel diffusion-tensor MRI approach for skeletal muscle fascicle length measurements. Physiol Rep 4(24):e13012. https://doi.org/10.14814/phy2.13012
Pullan AJ, Buist ML, Cheng LK (2005) Mathematically modelling the electrical activity of the heart: from cell to body surface and back again. World Scientific, Singapore. https://doi.org/10.1142/5859
Qu Z, Garfinkel A (1999) An advanced algorithm for solving partial differential equation in cardiac conduction. IEEE Trans Biomed Eng 46(9):1166–1168
Ramasamy E, Avci O, Dorow B, Chong SY, Gizzi L, Steidle G, Schick F, Röhrle O (2018) An efficient modelling-simulation-analysis workflow to investigate stump-socket interaction using patient-specific, three-dimensional, continuum-mechanical, finite element residual limb models. Front Bioeng Biotechnol 6:126
Röhrle O, Davidson JB, Pullan AJ (2012) A physiologically based, multi-scale model of skeletal muscle structure and function. Front Physiol 3:1–14
Röhrle O, Yavuz U, Klotz T, Negro F, Heidlauf T (2019) Multiscale modelling of the neuromuscular system: coupling neurophysiology and skeletal muscle mechanics. Wiley, Berlin
Rush S, Abildskov J, McFee R (1963) Resistivity of body tissues at low frequencies. Circ Res 12(1):40–50
Saad Y, Schultz MH (1986) Gmres: a generalized minimal residual algorithm for solving nonsymmetric linear systems. SIAM J Sci Stat Comput 7(3):856–869. https://doi.org/10.1137/0907058
Sbriccoli P, Sacchetti M, Felici F, Gizzi L, Lenti M, Scotto A, De Vito G (2009) Non-invasive assessment of muscle fiber conduction velocity during an incremental maximal cycling test. J Electromyogr Kinesiol 19(6):e380–e386
Shampine LF, Reichelt MW (1997) The matlab ode suite. SIAM J Sci Comput 18(1):1–22
Shorten PR, O'Callaghan P, Davidson JB, Soboleva TK (2007) A mathematical model of fatigue in skeletal muscle force contraction. J Muscle Res Cell Motil 28(6):293–313
Sinha U, Yao L (2002) In vivo diffusion tensor imaging of human calf muscle. J Mag Reson Imaging 15(1):87–95. https://doi.org/10.1002/jmri.10035
Sundnes J, Lines GT, Tveito A (2005) An operator splitting method for solving the bidomain equations coupled to a volume conductor model for the torso. Math Biosci 194:233–248
Sundnes J, Nielsen BF, Mardal K, Cai X, Lines GT, Tveito A (2006) On the computational complexity of the bidomain and the monodomain models of electrophysiology. Ann Biomed Eng 34(7):1088–1097. https://doi.org/10.1007/s10439-006-9082-z
Tung L (1978) A bi-domain model for describing ischemic myocardial dc potentials. PhD thesis, Massachusetts Institute of Technology
Whiteley JP (2006) An efficient numerical technique for the solution of the monodomain and bidomain equations. IEEE Trans Biomed Eng 53(11):2139–2147